# Optimization of the High-Frequency Radar Sites in the Bering Strait Region

GLEB PANTELEEV

*International Arctic Research Center, University of Alaska Fairbanks, Fairbanks, Alaska, and National
Research Tomsk Polytechnic University, Tomsk, Russia*

MAX YAREMCHUK

*Naval Research Laboratory, Stennis Space Center, Mississippi*

JACOB STROH

*University of Alaska Fairbanks, Fairbanks, Alaska*

PAMELA POSEY AND DAVID HEBERT

*Naval Research Laboratory, Stennis Space Center, Mississippi*

DMITRI A. NECHAEV

*University of Southern Mississippi, Hattiesburg, Mississippi*

(Manuscript received 2 April 2014, in final form 28 August 2014)

## ABSTRACT

Monitoring surface currents by coastal high-frequency radars (HFRs) is a cost-effective observational technique with good prospects for further development. An important issue in improving the efficiency of HFR systems is the optimization of radar positions on the coastline. Besides being constrained by environmental and logistic factors, such optimization has to account for prior knowledge of local circulation and the target quantities (such as transports through certain key sections) with respect to which the radar positions are to be optimized.

In the proposed methodology, prior information of the regional circulation is specified by the solution of the 4D variational assimilation problem, where the available climatological data in the Bering Strait (BS) region are synthesized with dynamical constraints of a numerical model. The optimal HFR placement problem is solved by maximizing the reduction of a posteriori error in the mass, heat, and salt (MHS) transports through the target sections in the region. It is shown that the MHS transports into the Arctic and their redistribution within the Chukchi Sea are best monitored by placing HFRs at Cape Prince of Wales and on Little Diomede Island. Another equally efficient configuration involves placement of the second radar at Sinuk (western Alaska) in place of Diomede. Computations show that 1) optimization of the HFR deployment yields a significant (1.3–3 times) reduction of the transport errors compared to nonoptimal positioning of the radars and 2) error reduction provided by two HFRs is an order of magnitude better than the one obtained from three moorings permanently maintained in the region for the last 5 yr. This result shows a significant advantage of BS monitoring by HFRs compared to the more traditional technique of in situ moored observations. The obtained results are validated by an extensive set of observing system simulation experiments.

## 1. Introduction

In recent years, the technology of monitoring coastal circulations by HF radars has improved considerably (Kohut and Glenn 2003; Kohut et al. 2012) and now routinely provides real-time maps of surface currents up to 250 km offshore (Harlan et al. 2010; Barrick et al. 2012; Abascal et al. 2012). Because of limitations in the number of continuously maintained high-frequency radars (HFRs), it is desirable to optimize their locations in such a way that HFR readings could be easily converted into robust estimates of the key circulation parameters [target quantities (TQs)].

*Corresponding author address:* Gleb Panteleev, University of Alaska Fairbanks, P.O. Box 757340, Fairbanks, AK 99775-7340.
E-mail: gleb@iarc.uaf.edu

The theory of optimal observations has been considered by many authors (e.g., Baker and Daley 2000; Köhl and Stammer 2004) and was used extensively in dynamical sensitivity studies (e.g., Marotzke et al. 1999; Losch and Heimbach 2007; Veneziani et al. 2009; Zhang et al. 2011) and optimization of in situ observations (Panteleev et al. 2009). The key idea is to explore the impact that small variations in the likelihood (cost) function attributed to new observation sites have on the a posteriori error variances of the optimized values of the TQs (e.g., velocity values, in particular locations or the mass, heat, and salt (MHS) transports through particular sections). Observation sites providing the largest impact on the TQs are assumed to be optimal in the sense that they provide the most information on the variability of TQs, and therefore most effectively reduce the a posteriori error variance after the corresponding data have been assimilated into a numerical model.

In the present study, we explore application of the four-dimensional variational data assimilation (4DVar) sensitivity technique to the problem of the optimal placement of HFRs. Performance of the method is assessed in the Bering Strait (BS) region, which is important from both academic and practical viewpoints. First, the anticipated growth of pan-Arctic transportation requires accurate assessment and forecasts of local circulation. From the academic point of view, the BS and the Chukchi Sea (CS) comprise the "hot spot" controlling the exchange of ice and seawater between the Pacific and Arctic Oceans. The impact of BS fluxes on the thermohaline structure of the Arctic Ocean (AO) depends on the redistribution of the Pacific heat and freshwater anomalies within the CS basin (Fig. 1). Both observational (Woodgate et al. 2005; Weingartner et al. 2005; Luchin and Panteleev 2014) and modeling (Winsor and Chapman 2004; Spall 2007; Watanabe and Hasumi 2009) studies suggest that Pacific waters enter the open AO through two pathways (Fig. 1): one following the Herald Canyon east of Wrangell Island and another through the Barrow Canyon between the Alaskan coast and Hanna Shoals. In the present study, transports through both pathways are selected [among the transports through other sections and the Bering Strait transport (BST) itself] as TQs used for optimizing the HFR positions.

Prior information of the local currents is specified by assimilating the available climatological data into a numerical model. Analysis of the dynamical balance in the assimilated model solution made by Panteleev et al. (2010) indicates that circulation variability in the BS region is governed by the wind-forced dynamics of a topographically controlled and geostrophically balanced barotropic flow.

This observation justifies monitoring the BST using HFR observations of surface currents and thus motivates
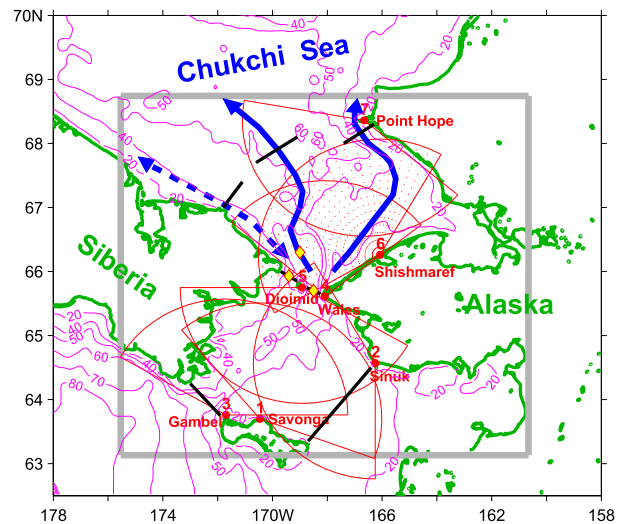


FIG. 1. Bathymetry of the BS region (pink contours, m) and the major pathways of Pacific waters (thick blue arrows). Dashed arrows show alternating coastal current north of the Chukchi Peninsula. Locations of the tested HFR sites (circles), sectors monitored by the HFRs, and their coverage by observation points (for Shishmareff location) are shown in red. Straight black lines denote MHS transport sections used for optimization of the HFR sites. Locations of the permanent NOAA moorings are shown by yellow diamonds. Boundary of the numerical model domain is given by the gray rectangle.

our optimization of HFR locations through dynamically constrained data assimilation combined with sensitivity analysis.

Such an approach for configuring long-term HFR observations may benefit the overall accuracy of measuring the exchange between the Arctic and Pacific Oceans under the constraints imposed by the limited number of logistically feasible monitoring sites in the region. True optimization of an HFR network involves many factors and guidelines that are difficult to express in mathematical terms. In the present study we limit ourselves by two principles: 1) the best (optimal) configuration maximizes the error reduction of a given set of TQs and 2) logistically permissible HFR sites are limited to the inhabited settlements on the Alaskan coast. Of course, there are many more guidelines and restrictions imposed by environmental, logistic, and financial conditions, and it is difficult to permanently define the set of TQs that will satisfy all the needs of the scientific, business, and local communities. Nevertheless, we assume that the proposed technique is worth considering as an element in the design of observational networks in the Arctic and in the Bering Strait in particular.

Historically, the BST has been estimated from moored observations conducted as early as the 1930s (Coachman and Aagaard 1966, 1988; Coachman et al. 1975), but its continuous monitoring began in 1990 with the deployment

of a mooring array as a part of a joint program between American and Russian scientists (Roach et al. 1995). Since that time, at least three moorings have been maintained in the BS region (Fig. 1), which provide a 20-yr series of the BST and associated MHS fluxes (Woodgate et al. 2005, 2012). In that context, it is instructive to compare the efficiency of monitoring the BST by a limited number of moorings and by a pair of optimally positioned HFRs.

Mathematically, the proposed optimization technique is applicable under the assumption that perturbations of the optimal state introduced by new observations are either small or that the state is governed by quasi-linear dynamics. For the large-scale circulation in the BS region, both assumptions appear to be acceptable for two reasons: First, as it was shown in Panteleev et al. (2010), the nonlinear terms in the governing equations are small compared to the wind forcing and geostrophy; second, the HFR observation errors (which include model representation errors) are larger than the respective surface velocity errors determined from the error analysis of the optimal state, which is constrained by massive in situ and remotely sensed observations.

In this study, the data-optimized climatological evolution of the ocean state in the BS region during the ice-free period (July–September) is used as a reference for optimization of HFR locations. The optimization criterion is the overall error reduction of the MHS transport estimates through a number of sections in the southern Chukchi and northern Bering Seas, including the Bering Strait. In the next section, we briefly describe the basic principles of optimizing the observations, the numerical model, and the methodology of the numerical experiments, including a description of the observing system simulation experiments (OSSEs) used to verify the results. Section 3 contains the results of HFR optimization together with recommendations for positioning of the HFRs on the U.S. coastline and comparison of the monitoring efficiencies of the BST by HFRs and by permanent moorings. A summary and a discussion in section 4 complete the paper.

## 2. Methodology

### a. Optimizing observations under the dynamical constraints

Consider an ocean general circulation model (OGCM) as a nonlinear mapping $\mathcal{N}$ of a vector of control parameters $\mathbf{c}$ to the ocean state $\mathbf{x}$:

$$\mathbf{x} = \mathcal{N}(\mathbf{c}). \tag{1}$$

Here, the $N$-dimensional ocean state vector $\mathbf{x} \in \mathcal{R}^N$ is composed of all the OGCM fields' values discretized on the four-dimensional space–time grid, while the control vector $\mathbf{c}$ contains poorly known input parameters of the model, which may include gridded fields of the initial and open boundary conditions, and the forcing fields.

Let $\mathbf{x}_o$ provide a minimum to some quadratic cost function $J(\mathbf{x})$ and $\delta\mathbf{x}$ be small deviations from $\mathbf{x}_o$. Then a variation $\delta J$ of $J$ from its value at the minimum is

$$\delta J = \frac{1}{2}\delta\mathbf{x}^T\mathbf{B}^{-1}\delta\mathbf{x} \equiv \frac{1}{2}\delta\mathbf{c}^T\mathbf{M}^T\mathbf{B}^{-1}\mathbf{M}\delta\mathbf{c}, \tag{2}$$

where $\mathbf{B}^{-1}$ is a nonnegative definite matrix and the superscript $^T$ stands for transposition. The symbol $\mathbf{M}$ here is the linearization of OGCM operator $\mathcal{N}$ in the vicinity of $\mathbf{c}_o$, the control vector mapped by $\mathcal{N}$ to $\mathbf{x}_o$, so that

$$\delta\mathbf{x} = \mathbf{M}\delta\mathbf{c} \tag{3}$$

holds.

The cost function [Eq. (2)] can be interpreted as the argument of a Gaussian probability density function. In this sense, $\mathbf{x}_o$ can be referred to as the "optimal" (most probable) state and $\mathbf{B}^{-1}$ is the inverse error covariance matrix.

Assume that $K$ additional observations $\mathbf{d}$ of the state vector $\mathbf{x}$ are made such that $\mathbf{d} = \mathbf{D}\mathbf{x} + \mathbf{e}$, where $\mathbf{e}$ is the observational noise with covariance $\mathbf{W}$ and $\mathbf{D}$ is the linear operator mapping of the state to observations. Given these new data, the variation of the cost function [Eq. (2)] should be augmented with the additional term

$$\delta J \rightarrow \delta J + \frac{1}{2}(\mathbf{D}\delta\mathbf{x} + \delta\mathbf{d})^T\mathbf{W}^{-1}(\mathbf{D}\delta\mathbf{x} + \delta\mathbf{d}), \tag{4}$$

where $\delta\mathbf{d} = \mathbf{D}\mathbf{x}_o - \mathbf{d}$ and $\delta\mathbf{x}$ is the perturbation of the optimal state caused by the cost function update. It follows from Eqs. (2) and (4) that the updated inverse error covariance is

$$\hat{\mathbf{B}}^{-1} = \mathbf{B}^{-1} + \mathbf{D}^T\mathbf{W}^{-1}\mathbf{D}. \tag{5}$$

Using the Woodbury identity, Eq. (5) can be rewritten in the form

$$\hat{\mathbf{B}} = \mathbf{B} - \mathbf{B}\mathbf{D}^T\hat{\mathbf{W}}^{-1}\mathbf{D}\mathbf{B}, \tag{6}$$

where

$$\hat{\mathbf{W}} = \mathbf{W} + \mathbf{D}\mathbf{B}\mathbf{D}^T. \tag{7}$$

Since both terms in the rhs of Eq. (6) are nonnegative definite, adding new observations always reduces the overall error variance described by the trace of $\hat{\mathbf{B}}$.

In oceanographic practice, observational arrays are often designed for monitoring certain quantities, such as MHS transports across key sections. By assuming that

a set of $m$ target quantities (TQs) $\mathbf{q} = \{q_1, \ldots, q_m\}$ is linearly related to the ocean state,

$$\mathbf{q} = \mathbf{Qx}, \qquad (8)$$

and taking Eq. (6) into the account, we can deduce that the total error variance of $\mathbf{q}$,

$$\mathbf{B}_q = \mathbf{QBQ}^\mathrm{T}, \qquad (9)$$

is reduced by

$$\mathrm{tr}\delta\mathbf{B}_q = \mathrm{tr}(\mathbf{B}_q - \hat{\mathbf{B}}_q) = \mathrm{tr}(\mathbf{QBD}^\mathrm{T}\hat{\mathbf{W}}^{-1}\mathbf{DBQ}^\mathrm{T}) = \mathrm{tr}(\mathbf{S}^\mathrm{T}\mathbf{S}). \qquad (10)$$

Here,

$$\mathbf{S} = \hat{\mathbf{W}}^{-1/2}\mathbf{DBQ}^\mathrm{T} \qquad (11)$$

is the sensitivity matrix (e.g., Köhl and Stammer 2004). By electing the trace of the covariance matrix as its norm, we employ the so-called A-optimality approach (e.g., Alvarez and Mourre 2012) commonly used in geosciences for optimal design of observational networks.

If $\mathbf{D}$ is the $N \times N$ identity matrix (i.e., full, direct state observation at all considered times), then the columns of $\mathbf{S}$ span the subspace of $\mathcal{R}^N$, whose elements affect the optimal values of $\mathbf{q}$. In particular, if $m = 1$, then there is a single TQ (e.g., transport through a section), and the sensitivity matrix is given by an $N$-dimensional vector $\mathbf{s}$. Since its square, $\mathbf{s}^\mathrm{T}\mathbf{s}$, gives the reduction of the error variance [Eq. (10)], plotting the 4D distribution of the absolute values of the components of s shows the relative contribution of the observations at various grid points to the reduction of the a posteriori error variance of the TQ. Therefore, the space–time locations of in situ observations with the largest impact on error variance reduction may be identified by inspecting the columns of $\mathbf{S}$. To simplify the visualization of the 4D sensitivities, their absolute values can be averaged over certain dimensions (e.g., over time) to produce "sensitivity maps" that show the relative contributions of various observation points in space to the overall error reduction (see section 3a).

In the considered case of HFR observations, a single radar measures projections of the surface currents on its beams at hundreds of locations (gray dots in Fig. 1), so that the operator $\mathbf{D}$ projects gridded velocity vectors of the model onto the beam directions at all $K$ observation points of the radar. A two-radar column of the sensitivity matrix is therefore $K_1 + K_2$ elements long, where $K_1$ and $K_2$ are the numbers of observation points monitored by the individual radars.

From the computational point of view, the most expensive part is obtaining the columns of the sensitivity matrix, mostly because of the huge size of $\mathbf{B}$. Furthermore, computing the action of $\mathbf{B}$ on a column $\mathbf{q}$ of $\mathbf{Q}^\mathrm{T}$ in Eq. (11) is not straightforward because the cost function [Eq. (2)] is formulated in terms of the sparse rank-deficient matrix $\mathbf{B}^{-1}$. This action may be calculated by inverting $\mathbf{B}^{-1}$ in the subspace spanned by control variable variations $\delta\mathbf{c}$. Using $\mathbf{B}_c$ to denote this inverse (i.e., the covariance $\overline{\delta\mathbf{c}\delta\mathbf{c}^\mathrm{T}}$) and taking Eq. (3) into the account, the relationship

$$\mathbf{B} = \overline{\delta\mathbf{x}\delta\mathbf{x}^\mathrm{T}} = \overline{\mathbf{M}\delta\mathbf{c}(\mathbf{M}\delta\mathbf{c})^\mathrm{T}} = \mathbf{MB}_c\mathbf{M}^\mathrm{T} \qquad (12)$$

is established, where overlines $[\overline{()}]$ denote the ensemble average. Term $\mathbf{B}_c$ has a significantly smaller dimension than $\mathbf{B}$ and its action on a control vector can be computed using the 4DVar code. Substitution of Eq. (12) into Eq. (11) yields the basic formula for computing the sensitivity matrix:

$$\mathbf{S} = \hat{\mathbf{W}}^{-1/2}\mathbf{DMB}_c\mathbf{M}^\mathrm{T}\mathbf{Q}^\mathrm{T}. \qquad (13)$$

To speed up the computations, $\mathbf{B}_c$ was approximated by the low-rank error covariance matrix retrieved from the data assimilative run of the Arctic Cap Hybrid Coordinate Ocean Model (AC/HYCOM) (section 2c).

The matrix $\mathbf{M}$ is implicitly given by the OGCM code linearized in the vicinity of the control vector associated with the model optimal state, both described in the next section. The code for computing the action of $\mathbf{M}^\mathrm{T}$ on a vector was available in the form of the adjoint model. The TQs were given by the set of the mean MHS fluxes through eight sections shown in Fig. 1. Mathematically, these fluxes are described by the integrals over the target sections $\sigma_i$ with $i = 1, \ldots, m$ as follows:

$$q_M^i = \left\langle \int_{\sigma_i} v \, d\sigma \right\rangle \qquad (14)$$

$$q_H^i = C_p \left\langle \int_{\sigma_i} v(\theta - \theta_0) \, d\sigma \right\rangle;$$

$$q_S^i = \left\langle \int_{\sigma_i} v(S - S_0) \, d\sigma \right\rangle, \qquad (15)$$

where angular brackets ($\langle \cdot \rangle$) denote time average, $v$ is the velocity component perpendicular to the $i$th section, $\theta$ is the seawater temperature, $S$ is salinity, and $C_p$ is the specific heat, where $\theta_0 = -1.9°\mathrm{C}$ and $S_0 = 34.8$ psu are the background values used for computing HS fluxes through the Bering Strait (e.g., Woodgate et al. 2012).

The rows $\mathbf{q}_i$ of the TQ matrix $\mathbf{Q}$ in Eq. (8) were computed by linearizing Eq. (15) in the vicinity of the reference state and then differentiating the finite-difference

analogs of Eqs. (14) and (15) with respect to all the gridpoint values of $v$, $\theta$, and $S$.

As a result, a column of **S** was computed in five steps:

1) Compute $\mathbf{q}' = \mathbf{M}^T\mathbf{q}$ by running the adjoint model forced by **q**.
2) Compute $\mathbf{c} = \mathbf{B}_c\mathbf{q}'$ by convolving the error covariance $\mathbf{B}_c$ between the control variables of the model with $\mathbf{q}'$.
3) Compute $\mathbf{x} = \mathbf{Mc}$ by running the tangent linear model forced by **c**.
4) Project **x** onto the observational points of a given pair of HFRs by computing the product $\tilde{\mathbf{x}} = \mathbf{Dx}$.
5) Rescale the result using multiplication by the inverse of the HFR measurement error: $\mathbf{s} = \hat{\mathbf{W}}^{-1/2}\tilde{\mathbf{x}}$.

In the following sections, we give more detail on the model **M** and estimations of the reference state and error covariance matrices $\mathbf{B}_c$ and $\hat{\mathbf{W}}$.

### b. Background state in the BS region

The reference state was found by assimilating the monthly averaged oceanographic (SST, temperature, salinity velocity, and ice observations) and atmospheric (NCEP reanalysis) data into the semi-implicit ocean model (SIOM). The monthly averaged temperature–salinity (T–S) data and corresponding variances were obtained by averaging over the model grid cells all of the available 17 960 temperature and 13 380 salinity profiles for July–September. The number of T–S profiles in some model grid boxes was insufficient to derive reliable estimates of data variance. In these cases, variability was represented by horizontal interpolations of statistics characterizing data variability. The obtained climatological data and the estimates of the corresponding standard deviations were used in the data assimilation procedure. The estimates of the monthly transports through the Bering Strait were taken from Woodgate et al. (2005).

Ice concentration from the NCEP reanalysis was used to set the model SST to the freezing value if the ice concentration exceeded the threshold value of 60%. NCEP–NCAR wind stress and surface heat–salt flux climatology (http://www.cdc.noaa.gov/cdc/data.ncep.reanalysis.derived.html) are too smooth for 8-km resolution. To allow for the adjustment of the spatial details in the model forcing, we used wind stress and heat–salt flux data with relatively high error variance, equal to 40% of their spatial and temporal variability in the northern BS and Chukchi Sea. This error level is consistent with the errors in the NCEP–NCAR forcing noticed by Ladd and Bond (2002).

The assimilation procedure is similar to the one used by Panteleev et al. (2007) to study the climatological circulation in the Kara Sea, and by Luchin and Panteleev (2014) to study climatological states in the Chukchi Sea, with the only difference being that the assimilated monthly climatologies (July–September) were derived for the BS region (Fig. 1) where the model was configured.

The SIOM is a modification of the C-grid, z-coordinate OGCM developed in the Laboratoire d'Oceanographie Dynamique et de Climatologié (Madec et al. 1998). The model was specifically designed for the implementation of 4DVar methods into regional simulations controlled by fluxes at the open boundaries and sea surface. The OGCM is semi-implicit with respect to both barotropic and baroclinic modes, permitting simulations with relatively large time steps of approximately 0.1 day (Nechaev et al. 2005; Panteleev et al. 2006a,b). The tangent linear model was obtained by direct differentiation of the forward model code. The adjoint code of the model was built analytically by transposition of the tangent linear model operator linearized in the vicinity of the given solution of the forward model. Further details of the SIOM's numerical scheme can be found in Nechaev et al. (2005).

In the present study, the computational grid has a horizontal resolution of 8 km, which is fine to resolve seasonal dynamics from a climatological perspective and coarse enough to suppress instabilities of the adjoint model at scales comparable with the local deformation radius (7 km). This permits use of a 2-month-long assimilation interval (from 16 July to 15 September) for integrating the model and its adjoint.

In the vertical dimension, the model has 13 unequally spaced layers ranging in thickness from 2.5 m at the surface to 10 m near the bottom. The maximum depth of the region is 86 m (Fig. 1). The model is controlled by the initial fields of temperature, salinity, velocity, and surface elevation (on 16 July), and by the three monthly-mean values of the same fields at the open boundaries. The number of gridded values of the control variables at the start of integration was 144 397. With the number of the gridded values of temperature, salinity, and velocity at the open boundaries equal to 13 389, the total number of control variables (dimension $n$ of the control vector **c**) is 157 786. The number of assimilated observations exceeded the number of control variables several times, rendering the assimilation problem relatively well determined.

Evolution of the reference state was obtained by finding the values of control variables that minimized the distance between the model fields and observations. The latter were specified once a day (every tenth time step) by linear interpolation of the three climatologies in time. With the total duration of 62 days (from the beginning of 16 July to the end of 15 September), there

were 63 time steps when observations were available. Fields at the model boundaries were specified in a similar manner by linear interpolation in time of the control values on day 1 (beginning of 16 July), day 31 (16 August), and day 62 (end of 15 September). Before the assimilation, these values were taken from the climatologies and then varied together with the initial fields (on 16 July) in the process of optimization.

As an example, evolution of the optimized sea surface temperature (SST) and velocity fields is shown in Fig. 2. The rms difference of the optimized temperature fields from the July and September climatologies (0.5°–0.9°C) lies well within the error bars. In addition, the optimized fields are constrained by the dynamics of the SIOM. Similar correspondence was found for the monthly-mean salinity fields. The evolution of the optimized Bering Strait transport (Fig. 3) shows the well-documented trend of the BST seasonal cycle (Woodgate et al. 2005, 2010, 2012), and it also fits the observational error bars (0.3 Sv) of Woodgate et al. (2005), shown by the vertical sides of the gray rectangles in Fig. 3. Optimized monthly-mean transport of freshwater and heat through the Bering Strait also demonstrate a similar consistence with the estimates of Woodgate et al. (2005), primarily because the model is constrained by the massive hydrological dataset (17 960 temperature and 13 380 salinity profiles) employed in the assimilation process.

Optimized transports through the other key sections (shown by straight black lines in Fig. 1) have also been checked against (rather scanty) estimates available in literature: The optimal summer transport of the Anadyr Current between the Chukchi Peninsula and St. Lawrence Island is $0.8 \pm 0.2$ Sv (where 1 Sv $\equiv 10^6$ m$^3$ s$^{-1}$) and is in good agreement with the estimate of Coachman (1993), who obtained the value of $0.7 \pm 0.2$ Sv from 1985 to 1988 current meter data.

The optimized flow pattern in the northern part of the model domain (Fig. 2c) agrees well with known schemes of the regional circulation (e.g., Winsor and Chapman 2004; Clement et al. 2005), revealing the central northward flow and flow through the Gulf of Kotzebue (solid blue arrows in Fig. 1). The ratio between the optimized transports of these branches (0.34 Sv/0.47 Sv) is in a good agreement with the ratio of the annual mean transports through the Herald Channel and the section between the Herald Shoal and Cape Lisburne obtained by Panteleev et al. (2010). The optimized circulation also reveals the well-known weak (~0.1 Sv) East Siberian Current (ESC) along the Siberian Coast (Weingartner et al. 1999).

Based on these comparisons against independent observations, we assume that the optimized solution realistically simulates the major features of the local
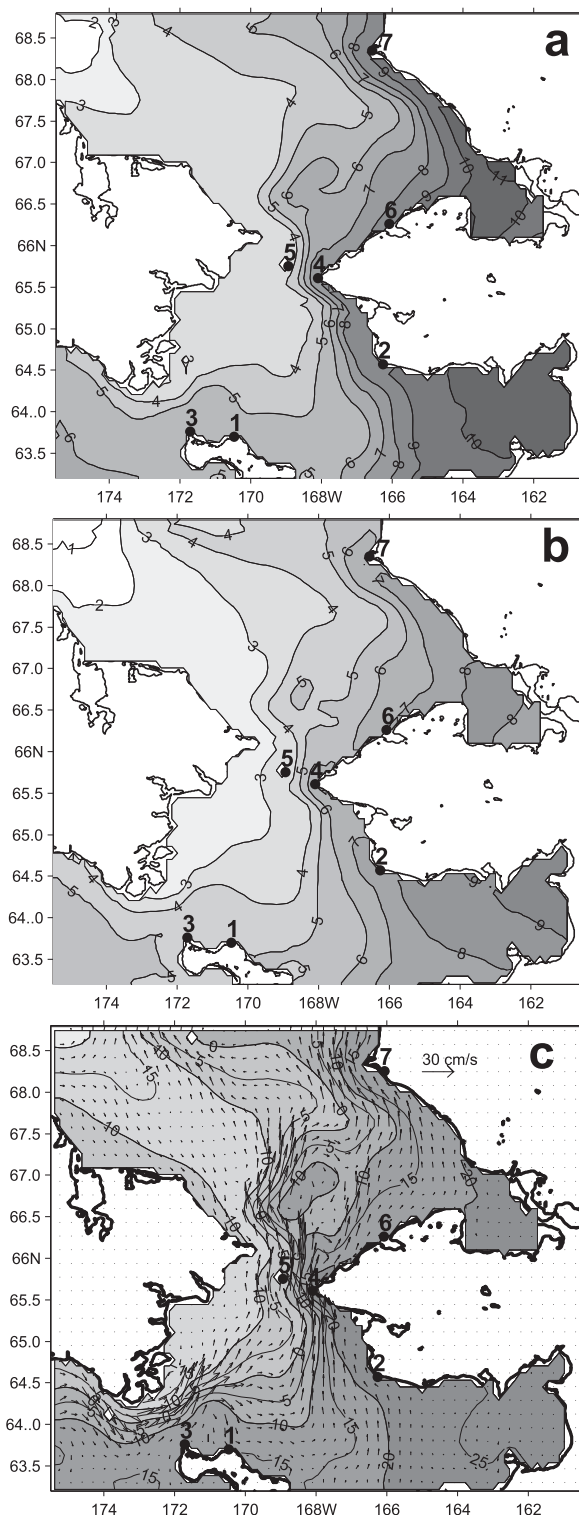


FIG. 2. SST (°C) of the reference state in (a) July and (b) September; and (c) the respective seasonal mean SSH (cm) and surface velocity fields. Every second arrow is shown.
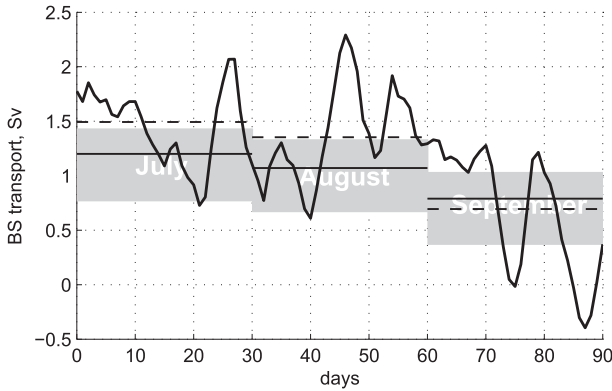
FIG. 3. Evolution of the AC/HYCOM BST averaged over two seasons—2011 and 2012 (thick solid line). Dashed lines are the monthly-mean values. Evolution of the monthly-mean SIOM transports is given by thin solid lines. Gray rectangles show the respective climatological estimates of Woodgate et al. (2005).



FIG. 4. Sea surface height (cm) and velocity at $z = 5$ m of the first eigenvector of the error covariance between the control variables corresponding to the initial conditions.

circulation in July–September and thus gives us grounds to use it as a background state $\mathbf{x}_o$ in the search for an optimal configuration of HFR sites.

### c. Estimation of the error covariances

To assess the error covariance of the reference state [$\mathbf{B}_c$ in Eq. (13)], we analyzed a multiyear run of an OGCM sequentially constrained by the data. For this purpose we used daily analyses together with the 12- and 24-h forecasts of the $1/12°$ AC/HYCOM (Posey et al. 2010; Allard et al. 2012) runs in July–September of 2011 and 2012. The error statistics was collected from the ensemble of differences between the AC/HYCOM analyses and the forecasts projected onto the SIOM grid. As a result, the ensemble had $k = 90$ days $\times 2 = 180$ daily sampled members. Since an ensemble member provides a sample of the error fields of the control variables, the sample error covariance in the control space $\mathbf{B}_c$ can be computed by

$$\mathbf{B}_c = \frac{1}{k-1} \mathbf{C}\mathbf{C}^{\mathrm{T}}, \qquad (16)$$

where $\mathbf{C}$ is the $k \times n$ matrix of the column-wise listed ensemble members with the ensemble means removed. As it is seen from Eq. (16), the $n \times n$ matrix $\mathbf{B}_c$ is strongly degenerate, as it has no more than $k - 1 \ll n$ non-0 eigenvalues. However, its product with a control vector requires only $2kn \ll n^2$ multiplications. To increase the computational efficiency, we performed a singular value decomposition of $\mathbf{B}_c$, which also gives insight into the spatial structure of the dominant error modes.

The spectrum of $\mathbf{B}_c$ computed with respect to the energy norm shows that the first eight eigenvectors account for 90% of the error variability. In the actual computations involving multiplication by $\mathbf{B}_c$ (e.g., step 2,
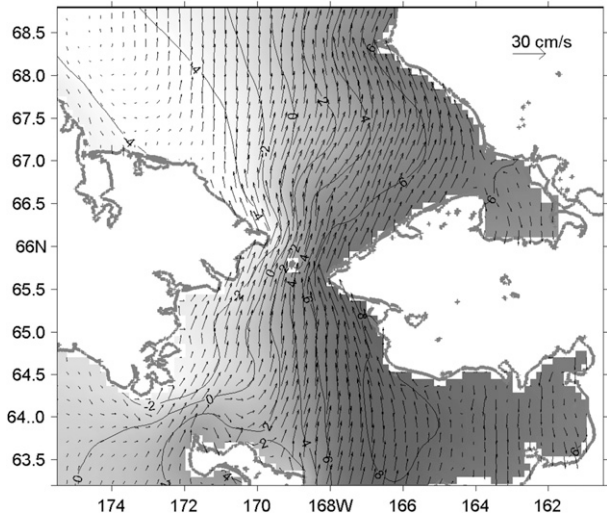
section 2a), we used 10 eigenvectors accounting for 93% of the total error estimated from the ensemble.

It is also instructive to analyze the leading eigenvectors of $\mathbf{B}_c$. Figures 4 and 5 show parts of the leading eigenvector that correspond to the initial conditions in sea surface height and velocity (Fig. 4), and the August mean values of the meridional velocity and temperature at the northern open boundary (Fig. 5). Figure 4 indicates that the leading error mode is close to geostrophic balance with somewhat larger uncertainties in the velocities along the U.S. side of the Bering Strait. Figure 5 demonstrates that errors in the Alaska Coastal Current (west-most part of the section) and the Herald Canyon flow (172°–173°W, see Fig. 1) tend to be negatively correlated. Temperature errors seem to be dynamically insignificant; supporting the notion that circulation in the region is predominantly barotropic in nature.

With the error covariance model [Eq. (16)] at hand, estimation of the second term in $\hat{\mathbf{W}} = \mathbf{W} + \mathbf{D}\mathbf{B}\mathbf{D}^{\mathrm{T}}$ [Eq. (7)] also becomes computationally feasible. We found that the rms error variances of the radial velocities extracted from the reference state varied within 2–4 cm s$^{-1}$ and therefore can be neglected compared to the HFR observational error variances $\mathbf{W}$, which have a typical magnitude of 5–15 cm s$^{-1}$. Taking this into account, the final approximation for the sensitivity matrix (13) has the form

$$\mathbf{S} = \mathbf{C}_r^{-1}\mathbf{V}^{-1}\mathbf{D}\mathbf{M}\mathbf{B}_c\mathbf{M}^{\mathrm{T}}\mathbf{Q}^{\mathrm{T}}, \qquad (17)$$

where $\mathbf{V}$ is the (diagonal) matrix of the HFR rms error variances and $\mathbf{C}_r$ is the square root of the HFR error correlation matrix.
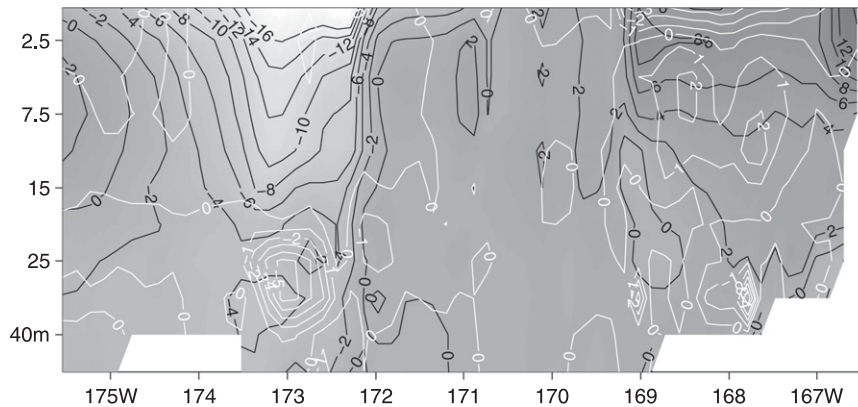
FIG. 5. Meridional velocity (black contours, cm s$^{-1}$) and temperature (white contours, 0.01°C) components of the first eigenvector of the error covariance between the control variables at the northern open boundary of the computational domain.

The error covariance model [Eq. (16)] also simplifies the estimation of the background error covariance matrix $\mathbf{B}_q$ [Eq. (9)] between the TQs. The magnitude of its trace provides a reference for assessing the relative rms error reduction $\xi_q$ in a specified set of target quantities $\mathbf{Q}$:

$$\xi_q = \left(\frac{\mathrm{tr}\delta\mathbf{B}_q}{\mathrm{tr}\mathbf{B}_q}\right)^{1/2} = \left[\frac{\mathrm{tr}(\mathbf{S}^\mathrm{T}\mathbf{S})}{\mathrm{tr}(\mathbf{Q}\mathbf{B}\mathbf{Q}^\mathrm{T})}\right]^{1/2}. \quad (18)$$

In this study, the three sets—$\mathbf{Q}_M$, $\mathbf{Q}_H$, and $\mathbf{Q}_S$—of target quantities are specified by the MHS transports through the sections shown in Fig. 1.

### d. HFR observations

Since the TQs used for optimization of HFR positions are characterized by a scale typically on the order of tens of kilometers, the HFR observational operators were chosen to mimic the long-range 5-MHz Coastal Ocean Dynamics Application Radar (CODAR) system (Barrick et al. 1977). This type of HFR employs two crossed-loop antennas around a whip (vertical monopole) as a receiving antenna and two whips as a transmitting antenna, and is capable of observing sea surface velocities up to 250 km offshore at radial, angular, and temporal resolutions of 6 km, 5°, and 20 min, respectively (Fig. 1).

Recent estimates of the CODAR radial velocity errors (e.g., Lipa 2003; Emery et al. 2004; Yoshikawa et al. 2006; Laws et al. 2010) indicate their variation from 3 to 4 cm s$^{-1}$ at small ranges to 15–20 cm s$^{-1}$ at 200–250 km. Based on this, we assumed a linear increase of the rms error variances with distance from the HFR base and adopted the following analytical model for the diagonal elements of the observation error variance matrix $\mathbf{V}$ in Eq. (17):

$$V_i = v_0(1 + r_i/r_0), \quad (19)$$

where $r_i$ is the distance of the $i$th observation point from the parent radar, $v_0 = 3\,\mathrm{cm\,s}^{-1}$, and $r_0 = 50\,\mathrm{km}$.

The direction-finding method (Lipa and Barrick 1983) employed by the CODAR system results in certain errors (3°–10°) in the bearing angle of the received signal. This property induces correlations between the radial velocity errors of the adjacent beams. To account for this, the entries of $\mathbf{C}_r$ were defined by

$$C_r^d = \exp(-d/r_1)\cos(\alpha_d). \quad (20)$$

Here $d$ is the distance between two observation points (not necessarily monitored by the same radar), $\alpha_d$ is the angle between the radial velocities observed in these points, and $r_1 = 10\,\mathrm{km}$.

In the experiments below, we consider only *pairs* of HFRs because single coastal radars are rarely deployed: the major purpose of such deployments is monitoring and prediction of the surface transport, which has many practical applications (search and rescue, pollution, etc.) and cannot be effectively carried out by observing only one velocity component. Considering more than two radars would require more voluminous computations, which, in principle, could be carried out, but lie beyond the scope of the present study, whose major objective is to demonstrate the performance of the sensitivity technique in application to the HFR deployment.

## 3. Results

### a. Impact of the surface velocity observations

Figure 6 demonstrates the time-averaged sensitivity (section 2a) of the mean Bering Strait mass transport to observations of surface velocities at the grid points of the
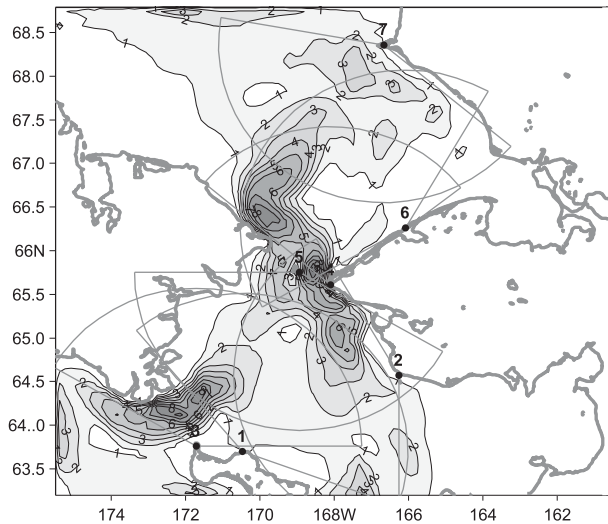
FIG. 6. Time-averaged sensitivity map of the mean BST to surface velocity observations. Sensitivity values are normalized by their maximum.

computational domain. The distribution was computed by setting **D** in Eq. (11) to have unit diagonal values for surface velocity components (i.e., surface velocity field observed in all grid points at all times) and zero otherwise. The map provides a qualitative insight for optimally positioning a pair of HFRs among the seven locations available within the existing U.S. settlements in the region (Fig. 1). Larger sensitivity values on the map correspond to regions where surface velocity observations provide a larger reduction of the a posteriori error variance of the BST. Ideally, a pair of radars should be positioned to cover the maximum possible area of the high-sensitivity regions in Fig. 6. These regions tend to align along the major currents contributing to the BST.

Examination of the maps in Figs. 1 and 3 shows that HFR placement at Cape Prince of Wales (CPW; point 4) and at Little Diomede Island (DI; point 5) are the best to cover the hot spots in the vicinity of the Bering Strait, whereas HFRs at Savonga (point 1) and Gambell (point 3) are able to cover the high-sensitivity patch associated with the Anadyr Current, around 64.2°N 172.3°W. HFR deployment at Shishmareff (point 6) or Point Hope (point 7) appears to be less efficient because radars at these locations are able to accurately monitor only the low-sensitivity areas (Fig. 6).

From the "common sense" point of view, one may argue that placement of radars close to the BS (at DI and CPW) should be the best because they measure the BS flow directly at the ranges of 30–60 km (i.e., with the highest accuracy). However, one should keep in mind that HFRs measure surface currents with large wave- and wind-driven components that are less correlated with the

long-term BST variations than the geostrophic component. In that respect simultaneous monitoring of the BST and the Anadyr Current south of the Chukchi Peninsula may provide more information about the mean BST by way of the geostrophically induced horizontal correlations between the surface currents at 64°–64.5°N, 170°–174°W and the BST.

Furthermore, the problem of optimal positioning becomes much more difficult if we consider a large set of the TQs, such as MHS transports through multiple sections shown in Fig. 1. In such a complex situation, the optimization approach described in section 2 may provide useful guidance for configuring HFR networks.

### b. Optimal HFR locations

Using the algorithm described in section 2a, a series of numerical experiments with pairs of HFRs virtually deployed in the seven settlements shown in Fig. 1 were conducted. All HFRs had identical characteristics: the aperture of 150° and the range of 200 km with the middle beam oriented perpendicular to the coastline. The only exceptions were the CPW (point 4) and DI (point 5) locations, where the northward and southward orientations of the middle beam were considered. The observation errors of the radars were assumed to be described by Eqs. (19) and (20). The azimuthal and radial resolutions were 5° and 6 km, respectively.

Figure 7 shows the values of the relative error reductions—$\xi_q^M$, $\xi_q^H$, and $\xi_q^S$—for 36 different combinations of the HFR pairs. The thick gray curve for the mass transport variance reduction shows two distinctive peaks. The first one involves a pair of southward-looking HFRs positioned at CPW (point 4) and DI (point 5), capable of reducing errors in the mass transports by 6.3%. The second peak (6.0–5.9% reduction) corresponds to the HFR deployments in Sinuk (point 2) and either DI or CPW. This configuration provides more accurate monitoring of the U.S. part of the BST, which contributes 70%–80% to the total transport (Coachman et al. 1975; Coachman and Aagaard 1988). Overall, optimal HFR deployment provides 1.3–3 times better reduction of the transport errors compared to other configurations.

It is noteworthy that pairs involving the key northward-looking DI and CPW radars demonstrate somewhat smaller error reduction compared to southward-looking configurations. The increased efficiency of the southward-facing HFR is due to the longer residence time of observed information as it propagates through the computational domain, which allows longer residence of the observed information in the computational domain. Similar effects have been also obtained in the efficiency analysis of the hydrophysical surveys (e.g., Panteleev and Semyonov 1988; Panteleev et al. 2004).
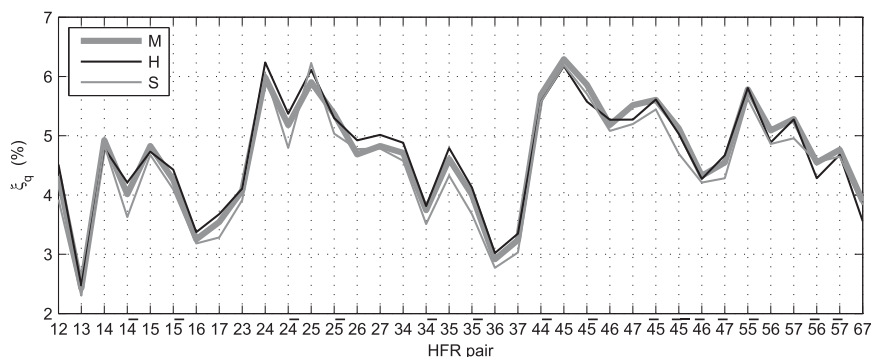
FIG. 7. Relative reduction $\xi_q$ of the errors in estimation of the MHS transports for various pairs of HFRs. Numbers labeling HFR pairs correspond to locations in Fig. 1. Bars over the CPW (point 4) and DI (point 5) locations denote northward-looking antennas at those sites.

It is also evident that compared to the volume transport, the curves for the heat and salt (HS) transports' error reduction demonstrate higher peaks for the Sinuk–DI and Sinuk–CPW pairs (6.3% and 6.1%, respectively). This can be explained by the fact that HS transports in July–September are particularly sensitive to variations in the temperature and salinity fields of the eastern part of the domain, where large riverine inflow of fresh and warm water from Alaska drive strong horizontal gradients (Fig. 2).

Pairs involving Shishmareff (point 6) and Point Hope (point 7) locations demonstrate lower values of $\xi_q$ in correspondence with the qualitative analysis of the sensitivity map in the previous section. The overall error reduction (computed by averaging the three curves in Fig. 7) gives a minor preference to the DI–CPW pair (6.3%), but its advantage over the Sinuk–CPW configuration (6.1%) may be insignificant given the uncertainties in the model and observational errors.

Interestingly, placement of the oppositely directed HFRs at DI and CPW ($4\overline{4}$ and $5\overline{5}$, respectively, configurations in Fig. 7) also results in a fairly good reduction of error ($\xi_q = 5.8\%$) despite the fact that HFR coverage areas do not intersect for these configurations. The result could be explained by the fact that such configurations cover a much larger area with strong sensitivities (Fig. 6) and weakly correlated (independent) observations. Such a choice of observation points is capable of providing a fairly large amount of information on the magnitude and redistribution of the BST because the measured radial velocities tend to be aligned in the principal direction of the flow.

Although the relative error reduction varies 2–3 times within the set of HFR pairs, the maximum magnitude error reduction may seem to be rather small (2%–6%) given the large amount of surface velocity data ($N \sim 3 \times 10^5$ observations) produced by a pair of radars in 3 months. However, the value of $N$ is still relatively small compared to the number of observations ($\sim 1.5 \times 10^6$) used for generating the reference state. Additionally, these observations cover all the components of the sea state (3D temperature, salinity, and velocity) and therefore formally define the seasonal mean values of the TQs with an accuracy that is high enough to restrict HFR data from providing a significant reduction of a posteriori error.

In that respect, it is instructive to compare the above-mentioned values of $\xi_q$ with the values provided by three moorings (Woodgate et al. 2012) permanently maintained in the region for the last 5 yr (Fig. 1). The corresponding computation is easily performed by changing HFR observational operators to operators that sample three vertical profiles of temperature, salinity, and velocity from the model fields at the mooring locations. The resulting values of $\xi_q$ appeared to be significantly (6–8 times) lower than those obtained for a pair of HFRs. This means that a limited number of moorings provide much less additional information about the TQs than a pair of HFRs. In other words, the key circulation features in the BS region could be better monitored by a pair of HFRs. This conclusion may seem intuitive because HFRs deliver much better spatial coverage at approximately the same temporal resolution. On the other hand, moored observational platforms provide information in the vertical, including temperature and salinity profiles, and, more importantly, are capable of operating under ice conditions.

Inspecting Fig. 7, one may also think that graphs reflect intuitive knowledge that is often used in planning oceanographic observations. We assume, however, that rigorous sensitivity and error analysis reflected in Figs. 5–7 may serve as a reasonable quantitative guidance in planning HFR observations in the Bering Strait region. For example, despite a somewhat smaller error reduction, oppositely directed HFR pairs at DI or CPW could be considered as reasonable alternatives to the best configurations (DI–CPW and Sinuk–CPW) because of the considerable savings in their maintenance costs.

To verify the above-mentioned results, a series of OSSEs was conducted.

### c. Validation of the results

The OSSE technique is widely used for skill assessment of the data assimilation systems. The underlying idea is to simulate artificial "data" using some reference model solution as a "true" ocean state, contaminate these data with noise (mimicking observational and model errors) to produce a "first guess" solution, and then try to reconstruct the "true state" from these data.

In the present study, the OSSEs were used to validate the optimized HFR locations obtained from the sensitivity analysis. "HFR data" were extracted from the reference solution described in section 2b. The first-guess solutions started from the geostrophically balanced state corresponding to the July climatology of temperature and salinity.

Next, simulated HFR data for a tested pair of locations were assimilated into the SIOM using the 4DVar algorithm with the same controls and data (excluding BS transport observations) that were used for optimization of the HFR locations.

The following model for the simulated HFR observations $v^*$ was adopted:

$$v^* = v + \mathbf{C}_r \mathbf{V} \mathbf{e}, \qquad (21)$$

where $v$ is the $K$-dimensional vector of the true projections of surface velocity on the HFR beams for a given pair of radars, and $\mathbf{e}$ is the noise from the standard normal distribution.

After assimilating the HFR data, transports through the sections in Fig. 1 were computed and the root-mean-square differences between the reconstructed transports and their values from the reference (true) solution were estimated. These mean differences and the corresponding difference for the BS transport were used as quantitative criterion to assess the quality of the tested pairwise HFR locations. Table 1 shows the results of the OSS experiments for several selected HFR pairs.

As it is seen from the table, there is a fairly good agreement between the OSSEs and the results of the sensitivity analysis at Fig. 7: the best HFR configurations are for the DI–CPW, Sinuk–CPW, and for the oppositely directed antennas on Little Diomede Island. The DI–Point Hope and Savonga–Sinuk pairs demonstrate significantly larger discrepancies, with the worst result provided by the Savonga–Gambel pair.

Although the rms difference between true and reconstructed volume transports can be considered as a reasonable quantification of error in the general circulation pattern, accuracy of the BS transport may be of

TABLE 1. Mean rms difference between the true and assimilated transports through the transects shown in Fig. 1, and absolute difference between the true and assimilated BST values. Optimization was done using the simulated data from HFR pairs.

| HFR pair | Mean error (Sv) | BST error |
|---|---|---|
| Diomede–CPW | 0.092 | 0.084 |
| Sinuk–CPW | 0.108 | 0.129 |
| Diomede–Diomede | 0.123 | 0.177 |
| Savonga–Sinuk | 0.192 | 0.285 |
| Savonga–Gambel | 0.246 | 0.454 |
| Diomede–Point Hope | 0.169 | 0.239 |

particular interest because of its strong correlation with ice and thermal conditions in the Chukchi Sea (Woodgate et al. 2010; Luchin and Panteleev 2014). The second column of the table shows the difference between reconstructed and true transports through the Bering Strait. Taking into account that the July–September mean BST is about 1 Sv, we can say that both DI–CPW and DI–Sinuk give rather accurate estimates of the BST, while positioning HFRs in Savonga–Sinuk or Savonga–Gambel cannot be considered as reasonable if the major goal is to obtain accurate estimates of the BST.

## 4. Summary and discussion

In this study, we comprehensively analyzed the impact of possible HFR locations on the accuracy of monitoring the MHS transports through the Bering Strait and their further distribution in the Chukchi Sea. The analysis is based on rigorous estimation of the a posteriori error reduction of the transports through eight sections under the dynamical constraints imposed by an OGCM. This is achieved using the so-called A-optimality criterion, which is based on reduction of the trace of the error covariance. We considered 36 realistic combinations of HFR pair deployment at existing Alaskan settlements.

Results of the study indicate that a pair of HFRs deployed at Little Diomede Island and Cape Prince of Wales provides the largest reduction ($\xi_q = 6.3\%$ on average) of the total MHS transport error. A similar reduction (6.1%) is obtained for HFRs at CPW and Sinuk. Northward-looking HFR antennas in CPW and Little Diomede Island showed a considerably (10%–20%) smaller error reduction in comparison to southward-looking antennas at those same sites. However, collocation of both a northward- and southward-looking antenna at DI or CPW (with $\xi_q = 5.8\%$) may be preferable for logistic reasons.

The velocity sensitivity maps obtained in the course of the analysis indicate that placement of a single mooring in the eastern channel of the Bering Strait is best in terms of error reduction of the MHS transports. This can be explained by the fact that the eastern channel is

much deeper than the western one (Fig. 1) and is characterized by stronger cross-strait variations of the temperature and salinity fields during the ice-free period considered here.

We also compared the efficiency of monitoring the target transports by the three moorings permanently maintained by NOAA in the region with the efficiency provided by the optimally placed pair of HFRs. Computations have shown a significant advantage of the HFR monitoring technique; the respective values of $\xi_q$ were 6–8 times larger for the HFRs. On the other hand, moored observational platforms provide information in the vertical, and, more importantly, are capable of operation under ice conditions when HFRs yield no measurements. For these reasons, it is highly desirable to complement the existing moorings by HFRs that have the potential to significantly increase the accuracy of TQ estimates during the ice-free season.

The technique used here can also be applied to optimization of multiple radars combined with permanent mooring deployments. In this case, the amount of computations will increase significantly, since a mooring may be placed at a much larger number of points than a radar station. However, these computations are quite feasible given that they are easily parallelizable and inexpensive; computation of $\delta\mathbf{B}_q$ for a single TQ and a given pair of HFRs consumed 2.5 CPU minutes on a laptop.

In that respect, an important issue is development of a general algorithm maximizing $\xi_q$ with respect to variations of the observation operator D, whose structure depends not only on the location of the observational platform but on its configuration (such as tunable antenna parameters in the case of HFRs). In the present study we immensely simplified the task by considering only a limited number of logistically feasible locations that allowed for a solution to the problem by brute force. In the more general formulation, it would be necessary to develop effective algorithms to seek a maximum of $\xi_q$ with respect to continuously varying parameters.

Nevertheless, we believe that the results of this study may serve as guidance for future planning of an HFR network in the Bering Strait region, although permanent HFR positions also depend on seasonal ice cover and other considerations not taken into account in the analysis. It may also be argued that the results could be model dependent. We believe, however, that such dependence may introduce only minor corrections because the July–September reference state used in our model is robust and statistically consistent with observations.

In general, the proposed technique could be applied to the design of observing systems in the hot spots of the World Ocean with typical scales (100–200 km) limited by areal coverage of the long-range HFR systems. We believe

that increasing the efficiency of the observing systems in these regions will remain one of the major scientific tasks in the near future that will promote further development and application of the methods described in this study.

## REFERENCES

Abascal, A. J., S. Castanedo, V. Fernández, and R. Medina, 2012: Backtracking drifting objects using surface currents from high-frequency radar. *Ocean Dyn.,* **62,** 1073–1089, doi:10.1007/s10236-012-0546-4.

Allard, R., and Coauthors, 2012: The Arctic Cap Nowcast Forecast System. *Geophysical Research Abstracts,* Vol. 14, Abstract EGU2012-2160. [Available online at http://meetingorganizer.copernicus.org/EGU2012/EGU2012-2160.pdf.]

Alvarez, A., and B. Mourre, 2012: Optimum sampling designs for a glider-mooring observing network. *J. Atmos. Oceanic Technol.,* **29,** 601–612, doi:10.1175/JTECH-D-11-00105.1.

Baker, N., and R. Daley, 2000: Observation and background adjoint sensitivity in the adaptive observation-targeting problem (2007). *Quart. J. Roy. Meteor. Soc.,* **126,** 1431–1454, doi:10.1002/qj.49712656511.

Barrick, D. E., M. W. Evans, and B. L. Weber, 1977: Ocean surface currents mapped by radar. *Science,* **198,** 138–144, doi:10.1126/science.198.4313.138.

——, V. Fernandez, M. Ferrer, C. Whelan, and C. Breivik, 2012: A short-term predictive system for surface currents from a rapidly deployed coastal HF radar network. *Ocean Dyn.,* **62,** 725–740, doi:10.1007/s10236-012-0521-0.

Clement, J. L., W. Maslowski, L. W. Cooper, J. M. Grebmeier, and W. Walczowski, 2005: Ocean circulation and exchanges through the northern Bering Sea—1979–2001 model results. *Deep-Sea Res. II,* **52,** 3509–3540, doi:10.1016/j.dsr2.2005.09.010.

Coachman, L. K., 1993: On the flow field in the Chirikov Basin. *Cont. Shelf Res.,* **13,** 481–508, doi:10.1016/0278-4343(93)90092-C.

——, and K. Aagaard, 1966: On the water exchange through the Bering Strait. *Limnol. Oceanogr.,* **11,** 44–59, doi:10.4319/lo.1966.11.1.0044.

——, and ——, 1988: Transports through the Bering Strait: Annual and interannual variability. *J. Geophys. Res.,* **93,** 15 535–15 539, doi:10.1029/JC093iC12p15535.

——, ——, and R. B. Trip, 1975: *Bering Strait: The Regional Physical Oceanography*. University of Washington Press, 172 pp.

Emery, B. M., L. Washburn, and J. A. Harlan, 2004: Evaluating radial current measurements from CODAR high-frequency radars with moored current meters. *J. Atmos. Oceanic Technol.,* **21,** 1259–1271, doi:10.1175/1520-0426(2004)021<1259:ERCMFC>2.0.CO;2.

Harlan, J., E. Terrill, L. Hazard, C. Keen, D. Barrick, C. Whelan, S. Howden, and J. Kohut, 2010: The Integrated Ocean Observing System high-frequency radar network: Status and

local, regional, and national applications. *Mar. Technol. Soc. J.,* **44,** 122–132, doi:10.4031/MTSJ.44.6.6.

Köhl, A., and D. Stammer, 2004: Optimal observations for variational data assimilation. *J. Phys. Oceanogr.,* **34,** 529–542, doi:10.1175/2513.1.

Kohut, J. T., and S. M. Glenn, 2003: Improving HF radar surface current measurements with measured antenna beam patterns. *J. Atmos. Oceanic Technol.,* **20,** 1303–1316, doi:10.1175/1520-0426(2003)020<1303:IHRSCM>2.0.CO;2.

——, H. Roarty, E. Randall-Goodwin, S. Glenn, and C. Sage Lichtenwalner, 2012: Evaluation of two algorithms for a network of coastal HF radars in the Mid-Atlantic Bight. *Ocean Dyn.,* **62,** 953–968, doi:10.1007/s10236-012-0533-9.

Ladd, C., and N. A. Bond, 2002: Evaluation of the NCEP/NCAR reanalysis in the NE Pacific and the Bering Sea. *J. Geophys. Res.,* **107,** 3158, doi:10.1029/2001JC001157.

Laws, K., J. D. Paudaun, and J. Vesecky, 2010: Estimation and assessment of errors related to antenna pattern distortion in CODAR SeaSonde high-frequency radar ocean current measurements. *J. Atmos. Oceanic Technol.,* **27,** 1029–1043, doi:10.1175/2009JTECHO658.1.

Lipa, B., 2003: HF radar current velocity uncertainties. *Sea Technol.,* **44,** 81–94.

——, and D. E. Barrick, 1983: Least-squares methods for the extraction of surface currents from CODAR crossed-loop data: Application at ARSLOE. *IEEE J. Oceanic Eng.,* **8,** 226–253, doi:10.1109/JOE.1983.1145578.

Losch, M., and P. Heimbach, 2007: Adjoint sensitivity of an ocean general circulation model to bottom topography. *J. Phys. Oceanogr.,* **37,** 377–393, doi:10.1175/JPO3017.1.

Luchin, V., and G. Panteleev, 2014: Thermal regimes in the Chukchi Sea from 1941 to 2008. *Deep-Sea Res.,* **109,** 14–26, doi:10.1016/j.dsr2.2014.05.007.

Madec, G., P. Delecluse, M. Imbard, and C. Lévy, 1998: OPA8.1: Ocean general circulation model. IPSL Reference Manual Notes du Pôle Modélisation 11, 91 pp.

Marotzke, J., R. Giering, K. O. Zhang, D. Stammer, C. Hill, and T. Lee, 1999: Construction of the adjoint MIT general circulation model and application to Atlantic heat transport sensitivity. *J. Geophys. Res.,* **104,** 29 529–29 547, doi:10.1029/1999JC900236.

Nechaev, D., G. Panteleev, and M. Yaremchuk, 2005: Reconstruction of the circulation in the limited region with open boundaries: Circulation in the Tsushima Strait. *Okeanologiya,* **45,** 805–828.

Panteleev, G. G., and E. V. Semyonov, 1988: On the strategy of hydrological array measurements. *Okeanologiya,* **28,** 1032–1034.

——, B. deYoung, C. Reiss, and C. Taggart, 2004: Passive tracer reconstruction as a least squares problem with a semi-Lagrangian constraint: An application to fish eggs and larvae. *J. Mar. Res.,* **62,** 787–814, doi:10.1357/0022240042880846.

——, D. A. Nechaev, and M. Ikeda, 2006a: Reconstruction of summer Barents Sea circulation from climatological data. *Atmos.–Ocean,* **44,** 111–132, doi:10.3137/ao.440201.

——, P. Stabeno, V. A. Luchin, D. Nechaev, and M. Ikeda, 2006b: Summer transport estimates of the Kamchatka Current derived as a variational inverse of hydrophysical and surface drifter data. *Geophys. Res. Lett.,* **33,** L09609, doi:10.1029/2005GL024974.

——, A. Proshutinsky, M. Kulakov, D. A. Nechaev, and W. Maslowski, 2007: Investigation of summer Kara Sea circulation employing a variational data assimilation technique. *J. Geophys. Res.,* **112,** C04S15, doi:10.1029/2006JC003728.

——, M. Yaremchuk, and D. A. Nechaev, 2009: Optimization of mooring observations in the northern Bering Sea. *Dyn. Atmos. Oceans,* **48,** 143–154, doi:10.1016/j.dynatmoce.2008.11.004.

——, D. A. Nechaev, A. Proshutinsky, R. Woodgate, and J. Zhang, 2010: Reconstruction and analysis of the Chukchi Sea circulation in 1990–1991. *J. Geophys. Res.,* **115,** C08023, doi:10.1029/2009JC005453.

Posey, P., E. J. Metzger, A. Walcraft, R. Preller, O. M. Smetstad, and M. W. Phelps, 2010: Validation of the 1/12° Arctic Cap Nowcast Forecast System (ACNFS). Naval Research Laboratory Tech. Rep. NRL/MR/7320-10-9287, 55 pp.

Roach, A. T., K. Aagaard, C. H. Pease, S. S. Salo, T. Weingartner, V. Pavlov, and M. Kulakov, 1995: Direct measurements of transport and water properties through the Bering Strait. *J. Geophys. Res.,* **100,** 18 443, doi:10.1029/95JC01673.

Spall, M. A., 2007: Circulation and water mass transformation in a model of the Chukchi Sea. *J. Geophys. Res.,* **112,** C05025, doi:10.1029/2005JC003364.

Veneziani, V., A. C. Edwards, and A. Moore, 2009: A central California coastal ocean modeling study: 2. Adjoint sensitivities to local and remote forcing mechanisms. *J. Geophys. Res.,* **114,** C04020, doi:10.1029/2008JC004775.

Watanabe, E., and H. Hasumi, 2009: Pacific water transport in the western Arctic Ocean simulated by an eddy-resolving coupled sea ice–ocean model. *J. Phys. Oceanogr.,* **39,** 2194–2211, doi:10.1175/2009JPO4010.1.

Weingartner, T. J., S. Danielson, Y. Sasaki, V. Pavlov, and M. Kulakov, 1999: The Siberian Coastal Current: A wind- and buoyancy-forced Arctic coastal current. *J. Geophys. Res.,* **104,** 29 697–29 713, doi:10.1029/1999JC900161.

——, K. Aagaard, R. Woodgate, S. Danielson, Y. Sasaki, and D. Cavalieri, 2005: Circulation in the north central Chukchi Sea shelf. *Deep-Sea Res. II,* **52,** 3150–3174, doi:10.1016/j.dsr2.2005.10.015.

Winsor, P., and D. C. Chapman, 2004: Pathways of Pacific water across the Chukchi Sea: A numerical model study. *J. Geophys. Res.,* **109,** C03002, doi:10.1029/2003JC001962.

Woodgate, R. A., K. Aagaard, and T. Weingartner, 2005: Monthly temperature, salinity, and transport variability of the Bering Strait through flow. *Geophys. Res. Lett.,* **32,** L04601, doi:10.1029/2004GL021880.

——, T. Weingartner, and R. Lindsay, 2010: The 2007 Bering Strait oceanic heat flux and anomalous Arctic sea-ice retreat. *Geophys. Res. Lett.,* **37,** L01602, doi:10.1029/2009GL041621.

——, ——, and ——, 2012: Observed increases in Bering Strait oceanic fluxes from the Pacific to the Arctic from 2001 to 2011 and their impacts on the Arctic Ocean water column. *Geophys. Res. Lett.,* **39,** L24603, doi:10.1029/2012GL054092.

Yoshikawa, Y., A. Masuda, K. Marubayashi, M. Ishibashi, and A. Okuno, 2006: On the accuracy of HF radar measurement in the Tsushima Strait. *J. Geophys. Res.,* **111,** C04009, doi:10.1029/2005JC003232.

Zhang, X., B. Cornuelle, and D. Roemmich, 2011: Adjoint sensitivity of the Niño-3 surface temperature to wind forcing. *J. Climate,* **24,** 4480–4493, doi:10.1175/2011JCLI3917.1.